

Cite this: *RSC Adv.*, 2018, 8, 29645

# Synthesis and photocatalytic properties of visible-light-responsive, three-dimensional, flower-like La–TiO<sub>2</sub>/g–C<sub>3</sub>N<sub>4</sub> heterojunction composites

Jinlong Li,<sup>a</sup> Lijuan Du,<sup>a</sup> Shuaiqiang Jia,<sup>a</sup> Guozhe Sui,<sup>a</sup> Yulin Zhang,<sup>a</sup> Yan Zhuang,<sup>a</sup> Boxin Li<sup>a</sup> and Zhiyong Xing<sup>\*b</sup>

We prepared a new three-dimensional, flower-like La–TiO<sub>2</sub>/g–C<sub>3</sub>N<sub>4</sub> (LaTiCN) heterojunction photocatalyst using a solvothermal method. Analysis and characterization were performed by conducting scanning electron microscopy, transmission electron microscopy, X-ray diffraction, X-ray photoelectron spectroscopy, Fourier transform-infrared spectroscopy, ultraviolet-visible spectrophotometry, and nitrogen adsorption and desorption. The prepared g–C<sub>3</sub>N<sub>4</sub> nanosheets could reach 100 nm in size and covered the TiO<sub>2</sub> surface. A tightly bound interface formed between the g–C<sub>3</sub>N<sub>4</sub> and TiO<sub>2</sub>, speeding up the effective transfer of photo-induced electrons. In addition, the incorporation of La<sup>3+</sup> reduced the electron–hole recombination efficiency. Consequently, the prepared La–TiO<sub>2</sub>/g–C<sub>3</sub>N<sub>4</sub> composite material exhibited better visible-light catalytic activity than pure TiO<sub>2</sub>.

Received 1st August 2018  
Accepted 14th August 2018

DOI: 10.1039/c8ra06466k

rsc.li/rsc-advances

## 1. Introduction

Photocatalytic degradation of organic pollutants and hydrogen production from water decomposition can improve the utilization of solar energy. Therefore, photocatalysis is considered to be an ideal green technology for solving the energy crisis and reducing environmental pollution.<sup>1,2</sup> In recent decades, TiO<sub>2</sub> and g–C<sub>3</sub>N<sub>4</sub> have been widely used in photocatalysis due to their non-toxicity, chemical stability and photocatalytic activity.<sup>3–5</sup> The close interface formed between the components of a composite semiconductor material can effectively promote the transport of photogenerated carriers, increasing the photocatalytic activity relative to those of pure semiconductors.<sup>6–8</sup> Therefore, the development of novel TiO<sub>2</sub>/g–C<sub>3</sub>N<sub>4</sub> heterojunction photocatalysts with excellent catalytic performance has become a topic of significant research interest.

Currently, most researchers use high-temperature calcination methods<sup>9–11</sup> or solvothermal methods<sup>12–14</sup> to recombine TiO<sub>2</sub> and g–C<sub>3</sub>N<sub>4</sub>. For instance, Chen *et al.*<sup>10</sup> heated modified TiO<sub>2</sub> particles and protonated g–C<sub>3</sub>N<sub>4</sub> particles at 70 °C to prepare a TiO<sub>2</sub>/Ag/g–C<sub>3</sub>N<sub>4</sub> composite microsphere with a particle size of 2–3 μm. Li *et al.*<sup>9</sup> prepared a TiO<sub>2</sub>/g–C<sub>3</sub>N<sub>4</sub> composite hollow sphere *via* a solvothermal method. In these TiO<sub>2</sub>/g–C<sub>3</sub>N<sub>4</sub> composite materials, g–C<sub>3</sub>N<sub>4</sub> is always uniformly attached to the TiO<sub>2</sub> particle surface and the composite particles exhibit

a uniform monodisperse relationship, but the particle size is within the micron range. Through the high-temperature calcination of a TiO<sub>2</sub> hollow sphere with a particle size of 50–100 nm and urea, Zou *et al.*<sup>15</sup> obtained a TiO<sub>2</sub>/g–C<sub>3</sub>N<sub>4</sub> composite material. However, TiO<sub>2</sub> microspherical particles can easily disperse in g–C<sub>3</sub>N<sub>4</sub> particles, mainly because it is difficult to control the bulk-g–C<sub>3</sub>N<sub>4</sub> coating on the surfaces of nanosized TiO<sub>2</sub> particles. To control this coating effectively and obtain a well-dispersed TiO<sub>2</sub>/g–C<sub>3</sub>N<sub>4</sub> composite material, the key is to prepare nanosized g–C<sub>3</sub>N<sub>4</sub> lamellae.

Adding metal ions can enable catalytic materials to absorb visible light more effectively.<sup>16–18</sup> It has been found that La is rich in electronic energy levels and that the introduction of electronic energy levels can reduce the energy gaps of catalytic materials and further increase the visible light absorption.<sup>19–21</sup> Rong *et al.*<sup>22</sup> reported that a g–C<sub>3</sub>N<sub>4</sub> photocatalyst doped with La exhibited higher photocatalytic activity in the degradation of organic pollutants. Khalid *et al.*<sup>23</sup> reported that a TiO<sub>2</sub>-graphene composite material doped with La resulted in remarkably slower electron–hole pair recombination than pure TiO<sub>2</sub>.

The main purposes of this study were to prepare a nanosized TiO<sub>2</sub>/g–C<sub>3</sub>N<sub>4</sub> composite material and further improve the photocatalytic activity of the TiO<sub>2</sub>/g–C<sub>3</sub>N<sub>4</sub> composite material by incorporating La<sup>3+</sup>. First, we prepared a g–C<sub>3</sub>N<sub>4</sub> nanosheet with plenty of nanopores *via* thermal spalling. Then, we achieved molecular self-assembly by employing a one-step solvothermal method and successfully prepared a La (x%)–TiO<sub>2</sub>/g–C<sub>3</sub>N<sub>4</sub> composite material with a three-dimensional, flower-like structure. During the molecular self-assembly process, the formed TiO<sub>2</sub> crystals acted as scissors, and the g–C<sub>3</sub>N<sub>4</sub> nanosheet was cut into increasingly smaller slices. Actually, the

<sup>a</sup>College of Chemistry and Chemical Engineering, Qiqihar University, Qiqihar 161006, China. E-mail: jinlong141@163.com; suiguozhe@163.com; Fax: +86-452-2738205; Tel: +86-452-2738205

<sup>b</sup>College of Science, Northeast Agricultural University, Harbin, 150030, China. E-mail: zyxing@neau.edu.cn; Fax: +86-451-55191810; Tel: +86-451-55191810

g-C<sub>3</sub>N<sub>4</sub> can also be loaded on many other semiconductors with matched energy band structure to construct high-efficient heterojunctions, and thus providing a new idea for fabricating g-C<sub>3</sub>N<sub>4</sub> based composite photocatalytic materials.

## 2. Experimental

### 2.1 Materials and chemicals

Melamine (C<sub>3</sub>H<sub>6</sub>N<sub>6</sub>) was used to synthesise the g-C<sub>3</sub>N<sub>4</sub> nanosheets. Tetrabutyl titanate (Ti(OC<sub>4</sub>H<sub>9</sub>)<sub>4</sub>) was utilized as the titanium precursor in the synthesis of nanocrystalline TiO<sub>2</sub>. Lanthanum nitrate (La(NO<sub>3</sub>)<sub>3</sub>·6H<sub>2</sub>O) was employed as the metal precursor for doping TiO<sub>2</sub>. These chemicals, together with hydrofluoric acid (HF, 40 wt%), ethanol (CH<sub>3</sub>CH<sub>2</sub>OH), sodium bicarbonate (NaHCO<sub>3</sub>), *tert*-butyl alcohol (C<sub>4</sub>H<sub>10</sub>O), *r*-benzoquinone (C<sub>6</sub>H<sub>4</sub>O<sub>2</sub>), and RhB (C<sub>28</sub>H<sub>31</sub>N<sub>2</sub>O<sub>3</sub>Cl), were of analytical grade and purchased from Sigma Aldrich Co. All of the reagents were of analytical grade and were used as obtained without further purification. Distilled water was employed in all of the experiments requiring water.

### 2.2 g-C<sub>3</sub>N<sub>4</sub> nanosheet preparation

Yellow bulk g-C<sub>3</sub>N<sub>4</sub> was obtained through the calcination of 5.0 g of melamine in a muffle furnace at a heating rate of 2 °C min<sup>-1</sup> at 550 °C for 4 h. After that, which was further oxidized and peeled off. The obtained light yellow powder was tiled in a square porcelain boat and calcined at a heating rate of 5 °C min<sup>-1</sup> at 530 °C for 2 h to obtain a white g-C<sub>3</sub>N<sub>4</sub> nanosheet.

### 2.3 La-TiO<sub>2</sub>/g-C<sub>3</sub>N<sub>4</sub> hybrid preparation

First, 0.6 g of g-C<sub>3</sub>N<sub>4</sub> nanosheet powder was added to 30 mL of anhydrous ethanol and ultrasonically dispersed for 2 h. Then, 3.0 mL of Ti(OC<sub>4</sub>H<sub>9</sub>)<sub>4</sub> was added to 20 mL of absolute ethanol to obtain a pale yellow transparent solution. La(NO<sub>3</sub>)<sub>3</sub>·6H<sub>2</sub>O was added stoichiometrically to dissolve the mixture completely into a transparent mixed solution and stirred for 30 min. The g-C<sub>3</sub>N<sub>4</sub> nanosheet dispersion was added to the Ti(OC<sub>4</sub>H<sub>9</sub>)<sub>4</sub> mixed solution and stirred for 30 min. Next, 1.5 mL of HF was pipetted dropwise into the resulting mixed solution and stirred for 15 min. The solution was then transferred to a 100 mL Teflon-lined high-value kettle and maintained at 160 °C for 20 h. It was subsequently cooled to room temperature, and the powder was washed several times with absolute ethanol and deionized water. The resulting sample was placed in a vacuum oven at 60 °C for 4 h. The atomic ratios of La to TiO<sub>2</sub> were 0.5%, 1%, and 2%. For comparison, the same method was used to prepare pure TiO<sub>2</sub>.

### 2.4 Photocatalytic activity evaluation

The photocatalytic activity of La (x%)-TiO<sub>2</sub>/g-C<sub>3</sub>N<sub>4</sub> (La<sub>x</sub>TiCN) in the degradation of RhB in aqueous solution was tested under visible light irradiation. A 500 W Xe lamp was employed as the light source, and the visible wavelength was adjusted using a 420 nm filter. For the experiments, 50 mg of La<sub>x</sub>TiCN and 50 mL of RhB solution (5 mg L<sup>-1</sup>) were added to the tube reactor. The suspension was magnetically stirred in the dark for 30 min prior to each assay so that it reached adsorption

equilibrium prior to irradiation. The samples were taken from the reactor at regular time intervals during irradiation and centrifuged using a high-speed centrifuge (RG-TGL-16C, Ruijiang Co.) to remove the photocatalyst. The samples were collected by centrifugation every 15 min to measure the RhB degradation by performing ultraviolet-visible (UV-vis) spectrophotometry, using the absorbance at 552.0 nm as the representative peak to determine the RhB concentration.

## 3. Results and discussion

### 3.1 Characterisation of synthesized catalysts

Fig. 1 shows the X-ray diffraction (XRD) patterns of TiO<sub>2</sub>, g-C<sub>3</sub>N<sub>4</sub>, TiO<sub>2</sub>/g-C<sub>3</sub>N<sub>4</sub> (TiCN), and La<sub>x</sub>TiCN. Evidently, the TiO<sub>2</sub> in all of the samples was of the anatase phase. The diffraction peaks at 25.3°, 38.0°, 48.0°, 54.1°, 62.6°, 69.6°, and 75.2° respectively correspond to the (101), (004), (200), (211), (204), (220), and (215) crystal faces of anatase (JCPDS-21-1272). Meanwhile, the peaks at 13.2° and 27.7° respectively correspond to the (100) and (002) crystal faces of g-C<sub>3</sub>N<sub>4</sub> (JCPDS no. 87-1526). In the composite samples of TiO<sub>2</sub>/g-C<sub>3</sub>N<sub>4</sub> and La<sub>x</sub>TiCN, the characteristic diffraction peaks of TiO<sub>2</sub> and g-C<sub>3</sub>N<sub>4</sub> are observable, indicating that TiO<sub>2</sub> and g-C<sub>3</sub>N<sub>4</sub> constituted a composite structure.<sup>24</sup> In addition, as compared with TiO<sub>2</sub>/g-C<sub>3</sub>N<sub>4</sub>, the diffraction peaks of La (x%)-TiO<sub>2</sub>/g-C<sub>3</sub>N<sub>4</sub> composite samples are not shifted higher or lower, indicating that La<sup>3+</sup> did not enter the TiO<sub>2</sub> lattice, because the ionic radius of La<sup>3+</sup> (0.115 nm) is much larger than that of Ti<sup>4+</sup> (0.064 nm), and La<sup>3+</sup> cannot replace Ti<sup>4+</sup> in a TiO<sub>2</sub> lattice and form lattice distortion,<sup>25</sup> which means that La<sup>3+</sup> ions may exist in the form of La<sub>2</sub>O<sub>3</sub> or LaF<sub>3</sub>. However, the relevant information about La<sub>2</sub>O<sub>3</sub> and LaF<sub>3</sub> is not observable, because the contents of La<sub>2</sub>O<sub>3</sub> and LaF<sub>3</sub> were relatively small. The lattice parameters of the samples were calculated from the XRD results, which are summarized in Table 1. Compared with the TiCN, the lattice parameters of La<sub>1</sub>TiCN were almost unchanged (a little decrease), which is consistent with the above results.

To demonstrate the formation of the La<sub>x</sub>TiCN sample heterostructure, scanning electron microscopy (SEM) and transmission electron microscopy (TEM) analyses were conducted.

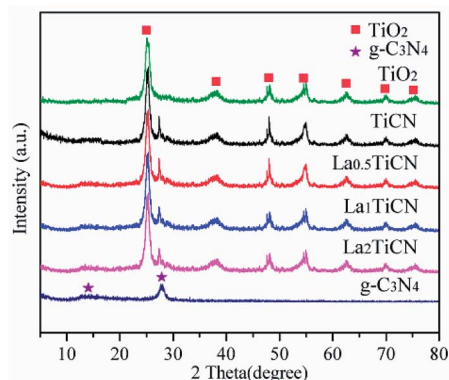


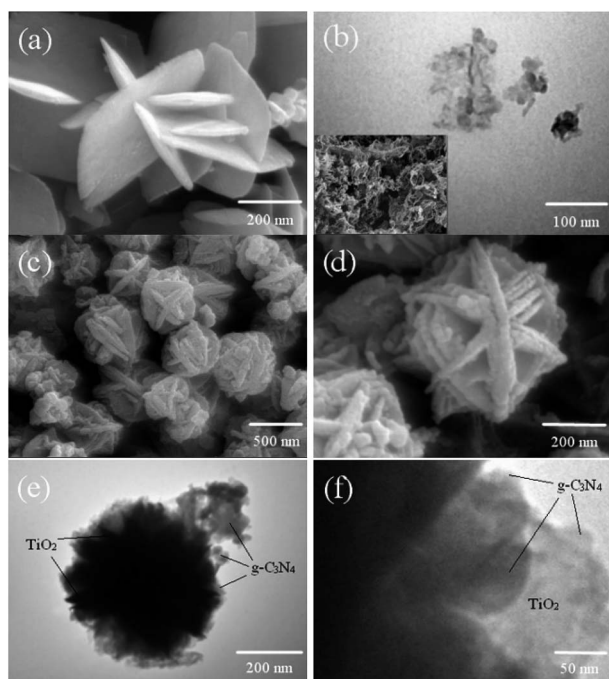
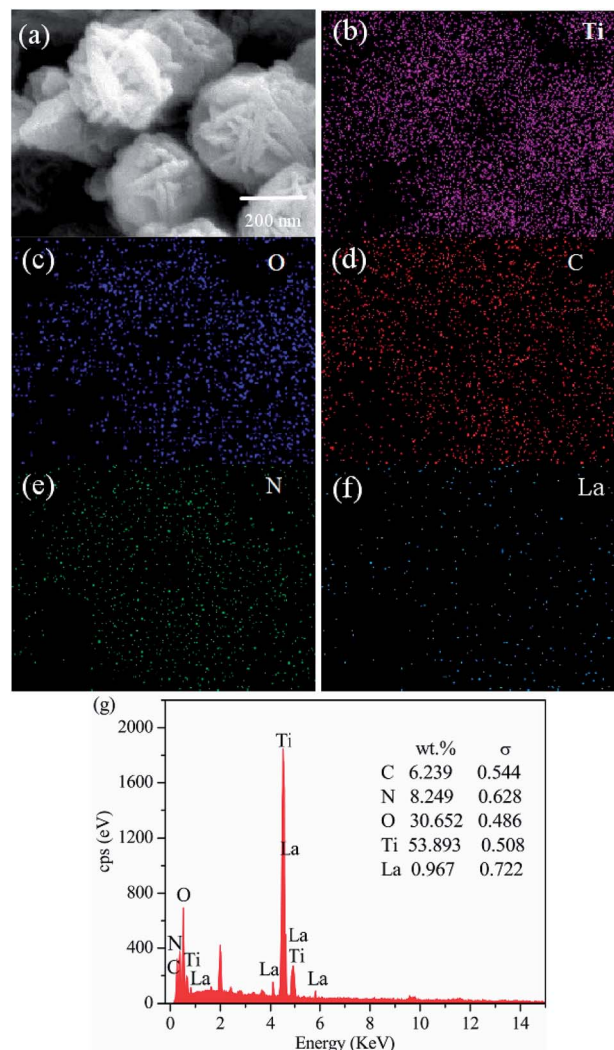
Fig. 1 XRD patterns of TiO<sub>2</sub>, g-C<sub>3</sub>N<sub>4</sub>, TiCN, and La<sub>x</sub>TiCN composites with various La contents.



**Table 1** The lattice parameters and the crystal size of the samples

Samples	$a = b$ (nm)	$c$ (nm)	Crystal size (nm)
$g\text{-C}_3\text{N}_4$	0.6412	0.2448	6.72
$\text{TiO}_2$	0.3786	0.9526	8.57
TiCN	0.3796	0.9512	8.52
$\text{La}_1\text{TiCN}$	0.3782	0.9508	7.66

Fig. 2a is the SEM diagram of pure  $\text{TiO}_2$ . The prepared  $\text{TiO}_2$  exhibits a three-dimensional, flower-like structure, which was formed by the staggered accumulation of 500 nm lamellae. Fig. 2b presents the TEM and SEM diagrams of  $g\text{-C}_3\text{N}_4$  that were obtained after secondary thermal spalling, displaying a structure with numerous pores. The size of the observed  $g\text{-C}_3\text{N}_4$  nanosheet is about 100 nm, enabling the  $g\text{-C}_3\text{N}_4$  to cover the  $\text{TiO}_2$  lamellae. Fig. 2c and d are SEM diagrams of the  $\text{La}_1\text{TiCN}$  composite material prepared by using the one-step solvothermal method. All of the sample particles exhibit three-dimensional, flower-like structures of the same size. Compared with pure  $\text{TiO}_2$ , the lamella surface of the flower-like structure of the  $\text{La}_1\text{TiCN}$  is coarser and the accumulation between lamellae is denser, which is probably due to the existence of the  $g\text{-C}_3\text{N}_4$  nanosheet, which provided more attachment points for the formation of  $\text{TiO}_2$  nanoparticles and enhanced the aggregation effect of the  $\text{TiO}_2$  nanoparticles during self-assembly. Fig. 2f is a TEM diagram of the  $\text{La}_1\text{TiCN}$  composite material, from which it is clear that  $g\text{-C}_3\text{N}_4$  nanosheet covers the surface of the  $\text{TiO}_2$  lamellae. The element mapping in Fig. 3 further proves the existence of elemental Ti, O, C, N, and La. It is evident that the Ti and O distribution diagrams can outline the basic shape of the three-dimensional,

**Fig. 2** SEM images of (a)  $\text{TiO}_2$ , (b) the  $g\text{-C}_3\text{N}_4$  nanosheet, and (c) and (d)  $\text{La}_1\text{TiCN}$ . (e) and (f) TEM images of  $\text{La}_1\text{TiCN}$ .**Fig. 3** (a) TEM image of the  $\text{La}_1\text{TiCN}$  sample. Corresponding energy-dispersive X-ray spectroscopy elemental mapping images of (b) Ti, (c) O, (d) C, (e) N, (f) La, and (g) EDX plots.

flower-like structure; the distributions of C and N are basically consistent with the material structure in Fig. 3d and e; and La is sparsely and evenly dispersed over the particle surface. The EDX spectrum confirms the presence of C, N, O, Ti, and La elements in  $\text{La}_1\text{TiCN}$  and the percentage of La is 1 wt% in Fig. 3g.

The amount of  $g\text{-C}_3\text{N}_4$  in the sample was determined by TG analysis. Fig. 4 shows a comparison of TG curves for  $g\text{-C}_3\text{N}_4$ , TiCN, and  $\text{La}_1\text{TiCN}$  samples. Pure  $g\text{-C}_3\text{N}_4$  has a large weight loss in the range of 500–700 °C. While TiCN and  $\text{La}_1\text{TiCN}$  lose weight rapidly in the same temperature range, which can be attributed to the combustion of  $g\text{-C}_3\text{N}_4$ . Therefore, the actual amount of  $g\text{-C}_3\text{N}_4$  in the TiCN and  $\text{La}_1\text{TiCN}$  samples were about 12.77 wt% estimating from the weight loss.

To determine the structural parameters of the synthesized samples, the  $\text{N}_2$  adsorption-desorption isotherms were measured in Fig. 5. The specific surface area of pure  $g\text{-C}_3\text{N}_4$  is 126.5  $\text{m}^2 \text{g}^{-1}$ , which mainly depends on the porous structure of  $g\text{-C}_3\text{N}_4$ . Compared with pure  $\text{TiO}_2$  (46.53  $\text{m}^2 \text{g}^{-1}$ ), the composite TiCN (62.75  $\text{m}^2 \text{g}^{-1}$ ), which is mainly produced by the





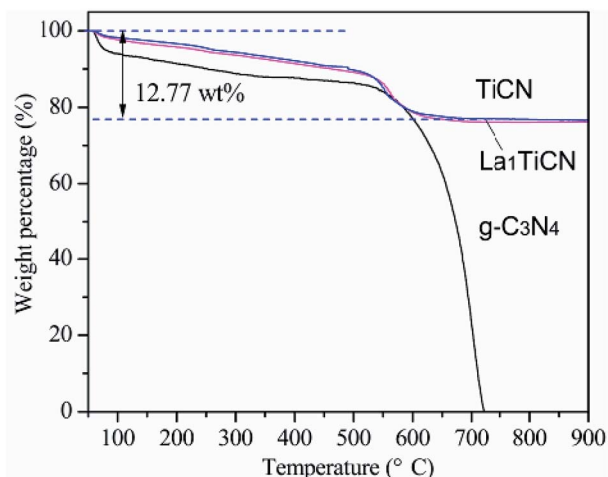


Fig. 4 TGA curves of  $g\text{-C}_3\text{N}_4$ , TiCN, and  $\text{La}_1\text{TiCN}$ .

deposition of the porous  $g\text{-C}_3\text{N}_4$  structure onto the  $\text{TiO}_2$  surface, provides a larger surface area. The surface area of  $\text{La}_1\text{TiCN}$  is  $72.77\text{ m}^2\text{ g}^{-1}$ , indicating that  $\text{La}^{3+}$  can increase the surface area of the catalyst and provide more reactive centres. Fig. 4b presents the pore size distribution curves of the samples. The pure  $g\text{-C}_3\text{N}_4$  pore size is 3.4 nm, while the  $\text{TiO}_2$  pore size is 5–12 nm. The main pore size of  $t\text{-La}_1\text{TiCN}$  presents a layered void composed of 3.8 nm (small pores) and 7.0 nm (larger mesopores). The existence of the layered void structure is beneficial to multi-light scattering/reflection, which greatly enhances the excitation.<sup>26</sup> In addition, a hierarchical porosity composed of mesopores facilitates fast mass transport, resulting in good electrode performance.<sup>27</sup> The similar effects from mesopores and a hierarchical porosity of the as-prepared  $\text{La}_x\text{TiCN}$  increase the photocatalytic activity.

The compositions and combination modes of the  $\text{TiO}_2$ ,  $g\text{-C}_3\text{N}_4$ , TiCN, and  $\text{La}_x\text{TiCN}$  samples were analysed by performing Fourier transform-infrared (FT-IR) spectroscopy. The results are shown in Fig. 6. For pure  $\text{TiO}_2$ , a strong absorption peak is evident at  $500\text{--}700\text{ cm}^{-1}$ , corresponding to the stretching vibrations of the Ti–O and Ti–O–Ti bands, and the two strong peaks at  $3350\text{--}3550\text{ cm}^{-1}$  and  $1645\text{ cm}^{-1}$  are attributable to the water and hydroxy absorbed by the  $\text{TiO}_2$  surface. In the pure  $g\text{-C}_3\text{N}_4$ , the absorption peaks at  $1239\text{ cm}^{-1}$ ,  $1317\text{ cm}^{-1}$ ,  $1407\text{ cm}^{-1}$ , and  $1571\text{ cm}^{-1}$  are attributable to the stretching vibrations of the C–N hybridized by  $\text{sp}^3$ ; the peak at  $1637\text{ cm}^{-1}$  is attributable to the stretching vibrations of C=N hybridized by  $\text{sp}^2$ ; and the peak at  $808\text{ cm}^{-1}$  corresponds to the out-of-plane bending vibrations of the 3-S-triazine units. For the TiCN and  $\text{La}_x\text{TiCN}$  composite samples, the main characteristic absorption peaks of  $\text{TiO}_2$  and  $g\text{-C}_3\text{N}_4$  are observable, indicating that the composite heterojunction structure of  $g\text{-C}_3\text{N}_4/\text{TiO}_2$  formed.<sup>28</sup> This finding is consistent with the X-ray diffraction (XRD) and X-ray photoelectron spectroscopy (XPS) results. Notably, compared with the patterns of the characteristic peaks of the pure  $g\text{-C}_3\text{N}_4$  nanosheet, those of the  $g\text{-C}_3\text{N}_4$  in the  $\text{La}_x\text{TiCN}$  composite sample are sharper, because the  $\text{La}_x\text{TiCN}$  composite sample had smaller  $g\text{-C}_3\text{N}_4$  lamellae than the pure

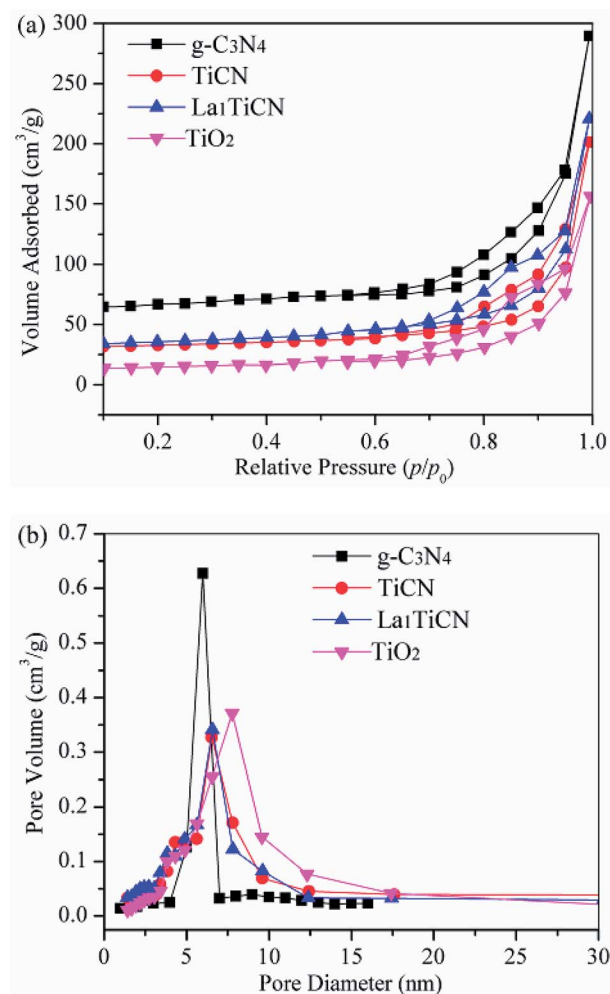


Fig. 5 (a)  $\text{N}_2$  adsorption–desorption isotherms of  $\text{TiO}_2$ ,  $g\text{-C}_3\text{N}_4$ , and  $\text{La}_1\text{TiCN}$  composites with various La contents and (b) pore size distributions of the corresponding samples.

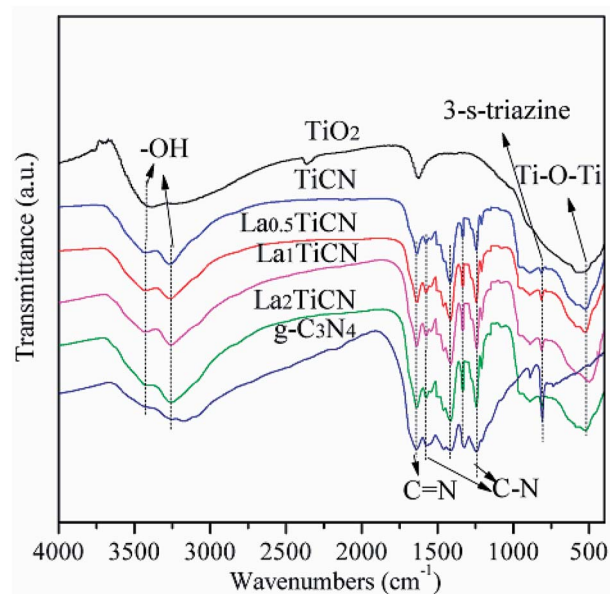


Fig. 6 FT-IR spectroscopy patterns of  $\text{TiO}_2$ ,  $g\text{-C}_3\text{N}_4$ , TiCN, and  $\text{La}_x\text{-TiCN}$  composites with various La contents.



g-C<sub>3</sub>N<sub>4</sub> nanosheet, causing the atoms in the g-C<sub>3</sub>N<sub>4</sub> neighbouring 3-*S*-triazine ring to separate from each other and weakening the interactions among the atoms. Therefore, the atoms in g-C<sub>3</sub>N<sub>4</sub> in the La<sub>x</sub>TiCN samples were under less constraining force, so the vibrations were stronger.<sup>29</sup>

Based on the analysis of the above experimental results, the formation mechanism of the La<sub>x</sub>TiCN heterojunction catalyst was determined and is depicted in Fig. 7. First, the Ti precursor micromolecule infiltrated the gaps among the g-C<sub>3</sub>N<sub>4</sub> lamellae. Then, the TiO<sub>2</sub> crystal grew on the lamella surface of g-C<sub>3</sub>N<sub>4</sub> and formed a sheet structure. The g-C<sub>3</sub>N<sub>4</sub> was divided into increasingly smaller lamellae, and La<sup>3+</sup> was deposited on the crystal surface. Finally, the obtained composite lamellae formed a La (x%)-TiCN heterojunction catalyst with a three-dimensional,

flower-like structure in a hydrotherm through self-assembly. During the formation of the samples, the generation of small g-C<sub>3</sub>N<sub>4</sub> through cutting during the formation of the TiO<sub>2</sub> crystal and through the formation of smaller g-C<sub>3</sub>N<sub>4</sub> particles was the key to the formation of the heterojunction structure.<sup>30</sup>

The chemical compositions of the prepared La<sub>x</sub>TiCN samples and the chemical states of all of the elements were analysed by performing XPS. Fig. 8a shows the full XPS results for the La<sub>1</sub>TiCN sample, where the spectral peaks of C 1s, N 1s, Ti 2p, O 1s, and La 3d are easily observable, indicating that the sample was mainly composed of C, N, Ti, O, and La. Notably, a weak F 1s peak is evident at 684.3 eV, which is probably attributable to the fluorination caused by the introduction of HF into the preparation process.<sup>31</sup>

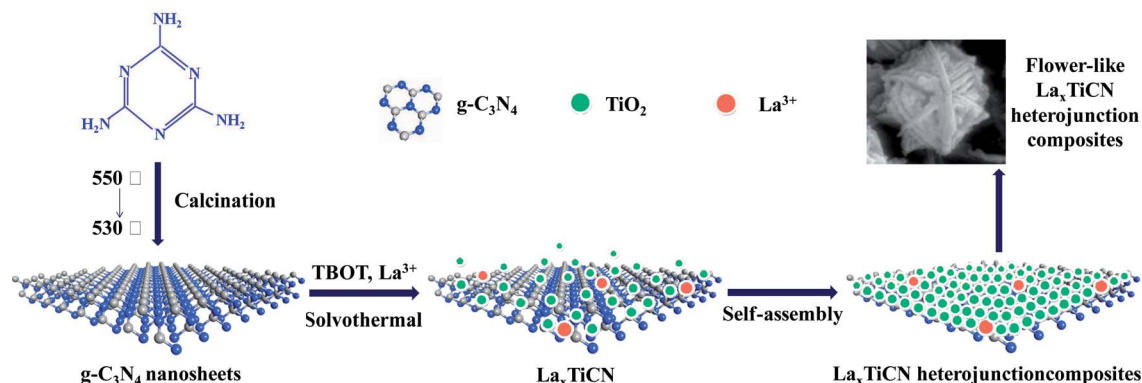


Fig. 7 Schematics illustrating La<sub>x</sub>TiCN formation.

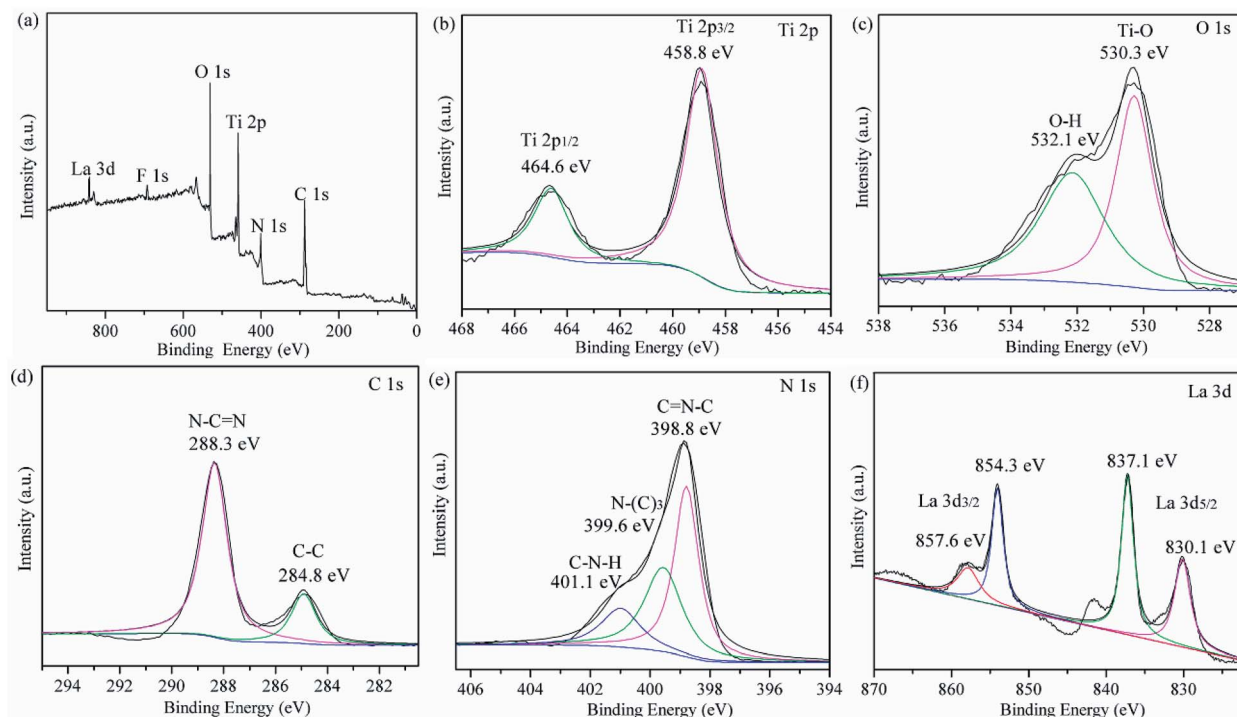


Fig. 8 (a) Overview of the XPS results and individual high-resolution XPS results for (b) Ti 2p, (c) O 1s, (d) C 1s, (e) N 1s, and (f) La 3d of as-prepared La<sub>1</sub>TiCN.



Fig. 8b presents the XPS results for Ti 2p, exhibiting two peaks at 459.4 eV and 465.1 eV, which respectively correspond to the Ti 2p<sub>3/2</sub> and Ti 2p<sub>1/2</sub> orbitals. Fig. 8c shows the XPS results for O 1s. The peak at 530.3 eV corresponds to Ti–O in the TiO<sub>2</sub> lattice, and that at 532.1 eV is attributable to the hydroxy or adsorbed water molecules on the sample surface. Fig. 8d presents the XPS results for C 1s, where there are two characteristic peaks at 284.8 eV and 288.3 eV, which are attributable to the C–C bands hybridized by sp<sup>3</sup> in g-C<sub>3</sub>N<sub>4</sub> and the N–C=N bands hybridized by sp<sup>2</sup>, respectively. Three peaks can be fitted from the XPS results for N 1s in Fig. 8e: C=N–C at 398.8 eV, N–(C)<sub>3</sub> at 399.6 eV, and C–N–H at 401.1 eV. In addition, no significant Ti–C (C 1s 283.0 eV)<sup>32</sup> or Ti–N (N 1s 399.3 eV)<sup>33,34</sup> signal is observable, and the binding energy of Ti 2p<sub>3/2</sub> does not shift lower,<sup>34</sup> indicating that atomic C and N were not incorporated into the TiO<sub>2</sub> lattice. An additional explanation is that the g-C<sub>3</sub>N<sub>4</sub> particles in the compound were only deposited on the surface of the TiO<sub>2</sub>, forming a hetero-junction structure.

Fig. 8f presents the XPS results for La 3d, showing peaks at 837.1 eV and 854.3 eV, which respectively correspond to La 3d<sub>5/2</sub> and La 3d<sub>3/2</sub>, as well as satellite peaks at 841.5 eV and 857.6 eV, which were respectively split by La 3d<sub>5/2</sub> and La 3d<sub>3/2</sub>. According to the literature, the characteristic peaks of La<sub>2</sub>O<sub>3</sub> are located at 834.9 eV and 851.8 eV,<sup>35</sup> indicating that La<sup>3+</sup> in the La<sub>x</sub>TiCN sample and elemental O with stronger electronegativity formed Ti–O–La, and the binding energy shifted higher.<sup>36</sup> These findings agree with the XRD results.

UV-vis diffuse reflectance spectrometry was then conducted to measure the absorbances of the samples. Fig. 9a shows the UV-vis diffuse reflection spectra of the g-C<sub>3</sub>N<sub>4</sub>, TiO<sub>2</sub>, TiCN, and La<sub>x</sub>TiCN composite catalysts. The absorption edge wavelengths of the pure TiO<sub>2</sub> sample and g-C<sub>3</sub>N<sub>4</sub> are about 390 nm and 460 nm, respectively. Compared with the absorption edge of the pure TiO<sub>2</sub> particles, that of the TiCN composite sample is shifted towards longer wavelengths and displays strong absorption in the 380–430 nm range, because the interface matching effect between TiO<sub>2</sub> and g-C<sub>3</sub>N<sub>4</sub> changed the optical properties of TiO<sub>2</sub>.<sup>37</sup> When doped with La<sup>3+</sup>, La<sub>0.5</sub>TiCN and La<sub>1</sub>TiCN display stronger visible light absorption in the 380–450 nm range. La<sub>1</sub>TiCN exhibits the best visible light absorption, while that of La<sub>0.5</sub>TiCN is slightly weaker, probably because the La<sup>3+</sup> concentration was too low and could not provide more electronic row traps.<sup>38</sup> Meanwhile, for the La<sub>2</sub>TiCN sample, the UV and visible light absorption are both significantly lowered, because an excessively high La<sup>3+</sup> concentration can reduce the light transmittance of the catalysts and light absorption efficiency.<sup>39</sup>

The band-gap energies of the samples were estimated by performing Kubelka–Munk conversion, and the results are shown in Fig. 8b. The band-gap energies of pure TiO<sub>2</sub>, g-C<sub>3</sub>N<sub>4</sub>, TiCN, and La<sub>1</sub>TiCN are respectively 3.00 eV, 2.50 eV, 2.78 eV, and 2.45 eV. The La<sub>1</sub>TiCN sample has a lower band-gap energy, probably because the introduction of La<sup>3+</sup> led to the formation of a new impurity energy level in the TiO<sub>2</sub> band gap, narrowing its band gap and extending its light absorption range.<sup>40</sup>

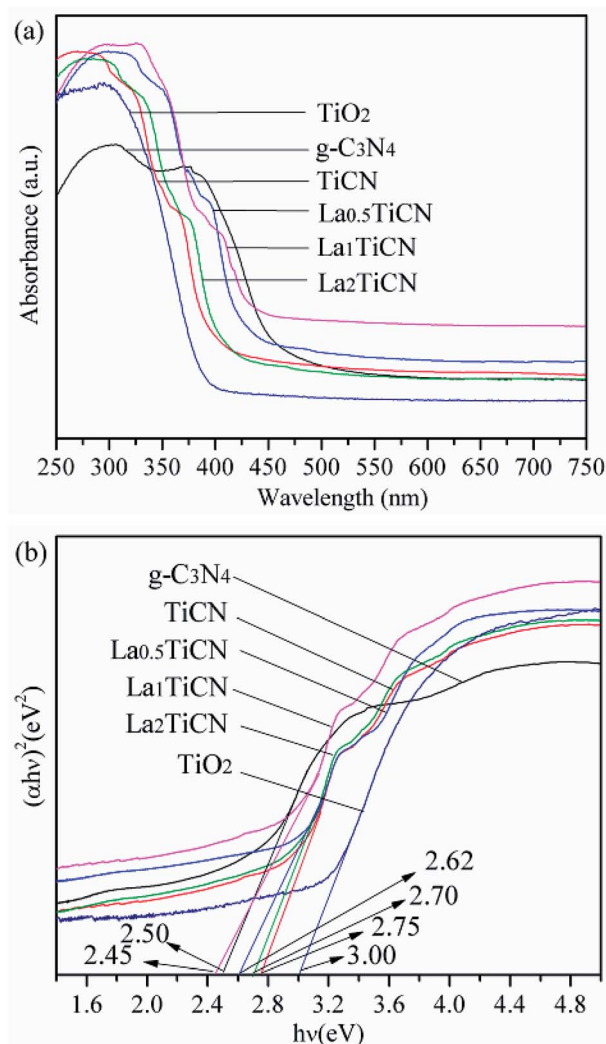


Fig. 9 (a) UV-vis diffuse reflection spectra and (b) plots of  $(\alpha hv)^2$  versus energy  $hv$  for the catalysts.

### 3.2 Photocatalytic activity and photodegradation mechanism

Under visible light irradiation, the photocatalytic efficiencies of the various samples were determined based on the RhB degradation, with the results shown in Fig. 10a. The photocatalytic activities of the various samples were further compared by using the equation  $\ln(C_0/C) = kt$ , where  $C_0$  is the initial RhB concentration,  $C$  is the instantaneous RhB concentration at time  $t$ , and  $k$  is the kinetic constant.

The first-order kinetic model of RhB degradation was obtained, with the results presented in Fig. 10b and the calculated  $k$  values given in Fig. 10c. Compared with the photocatalytic efficiencies of pure TiO<sub>2</sub> and g-C<sub>3</sub>N<sub>4</sub>, those of all of the La<sub>x</sub>TiCN composite samples are increasingly enhanced, mainly because the large and dense hetero interface formed between TiO<sub>2</sub> and g-C<sub>3</sub>N<sub>4</sub> could speed up the efficient electron–hole shifting. In addition, along with continuously increasing La<sup>3+</sup>, the photocatalytic efficiencies of the La<sub>0.5</sub>TiCN and La<sub>1</sub>TiCN samples are increasingly enhanced. The photocatalytic efficiency of La<sub>1</sub>TiCN





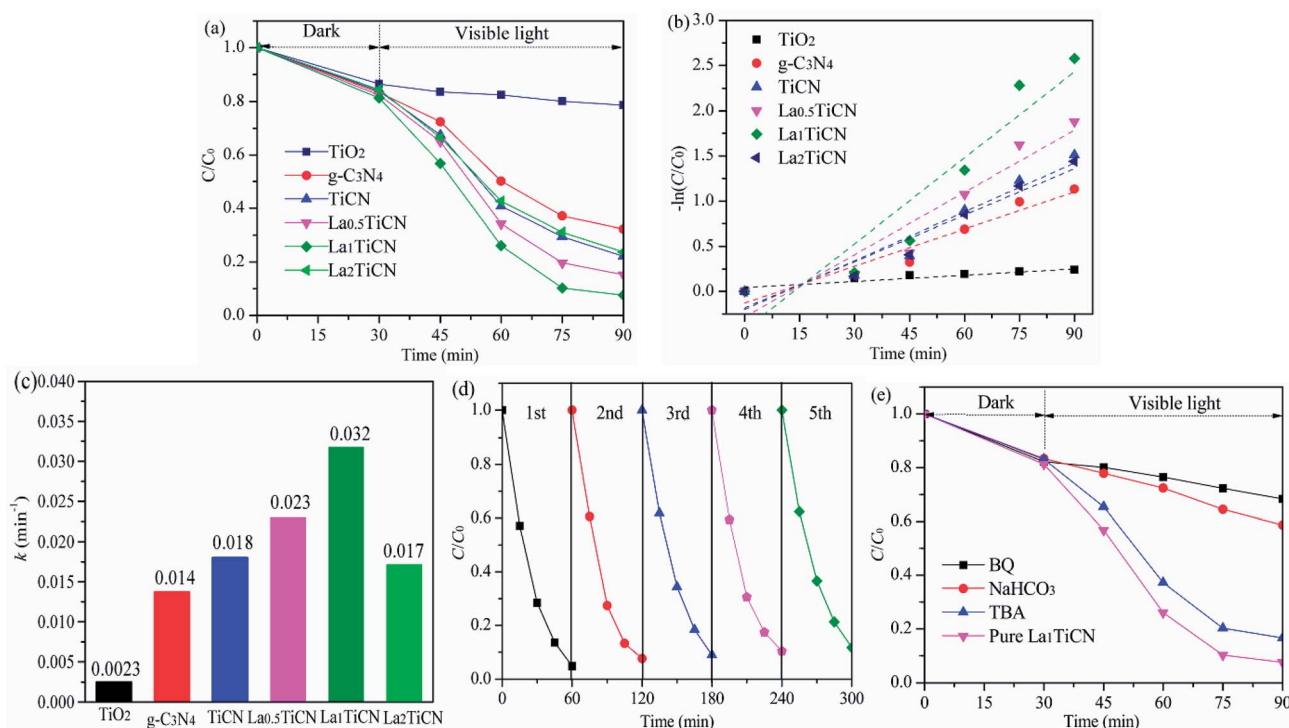


Fig. 10 (a) Photocatalytic degradation of RhB under visible light irradiation, (b) linear transforms  $-\ln(C/C_0)$  of the kinetic curves of RhB degradation, (c) apparent pseudo-first-order rate constant  $k_{app}$  with different catalysts, (d) recycling of the  $La_1TiCN$  in the removal of RhB dyes, and (e) scavenger test results obtained using  $La_1TiCN$ .

is 95.2%, and the kinetic constant is  $0.0325 \text{ min}^{-1}$ , which is 2.1 and 10 times those of pure  $TiO_2$  and  $g-C_3N_4$ , respectively, and 1.63 times that of  $La_xTiCN$ . Incorporating  $La^{3+}$  can firstly provide more electron traps and improve the electron-hole separation efficiency in  $La_1TiCN$ . In addition, incorporating  $La^{3+}$  can increase the specific surface area of  $TiCN$ , with the strongest photocatalytic effect. Notably, the photocatalytic effect of  $La_2TiCN$  is reduced, because excessive  $La^{3+}$  can serve as the recombination centre of electron-holes, reducing the photocatalytic activity of  $La_2TiCN$ . For evaluating the recyclability of the flower-like  $La_xTiCN$  heterojunction composites, cycling experiments were performed by washing the composite with ethanol for several times. As shown in Fig. 10d, the photocatalytic efficiency of RhB decreases from 95.2 to 88.3% for  $La_1TiCN$  after five cycles. This fact demonstrates that the obtained flower-like  $La_xTiCN$  heterojunction composites have good stability under visible-light irradiation and are less photo-corroded during the photocatalytic oxidation, which can be applied as a new option for dye wastewater treatment.

To determine the reactive species during a light-catalysed reaction, it is possible to eliminate holes  $h^+$ , superoxide radicals  $\cdot O_2^-$ , and hydroxyl radicals  $\cdot OH$  by adding  $NaHCO_3$ , BQ, and TBA. The obtained results are shown in Fig. 9d. It is evident that adding  $NaHCO_3$  and BQ significantly inhibited the light degradation of RhB in the  $La_1TiCN$  sample, indicating that under visible light irradiation,  $O_2^-$  and  $h^+$  are the main active substances in RhB photolysis. The equations  $E_{VB} = \chi - E_e + 0.5BG$  and  $E_{CB} = E_{VB} - BG$  were then employed to calculate the VB and CB potentials,  $E_{VB}$  and  $E_{CB}$ , respectively, where BG is the

band gap,  $\chi$  is the absolute electronegativity of the semiconductor, and  $E_e$  is the energy of free electrons based on the hydrogen scale and has a value of 4.50 eV.<sup>41</sup> For  $TiO_2$  and  $g-C_3N_4$ ,  $\chi$  is 5.81 and 4.72, respectively.

The VB and CB edge electric potentials of  $TiO_2$  and  $g-C_3N_4$  were calculated. The VB and CB edge potentials of  $TiO_2$  were determined to be +2.83 eV and -0.17 eV, respectively, and those of  $g-C_3N_4$  were found to be +1.47 eV and -1.03 eV, respectively.

Under visible light irradiation, the electrons from the VB of  $TiO_2$  and  $g-C_3N_4$  were respectively excited into the CB and left positively charged holes in the VB. Since the CB of  $g-C_3N_4$  (-1.03 eV) has a potential lower than that of  $TiO_2$  (-0.17 eV), the excited electrons on the  $g-C_3N_4$  surface can easily shift to the  $TiO_2$  surface through the hetero interface.<sup>42</sup> Finally, these

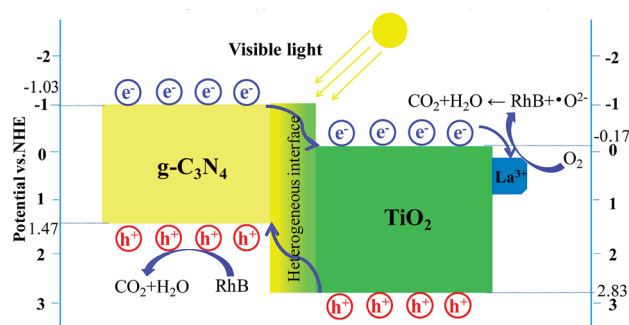


Fig. 11 Proposed visible light photodegradation mechanism of the  $La_1TiCN$  hybrid photocatalyst.



electrons can be captured by the  $\text{La}^{3+}$  with free orbitals.<sup>43</sup> The electrons accumulated on the  $\text{La}^{3+}$  surface can easily be captured by the  $\text{O}_2$  dissolved in solution to generate superoxide  $\cdot\text{O}^{2-}$ , and the generated  $\cdot\text{O}^{2-}$  can subsequently be used to degrade RhB. Similarly, the holes in the VB of  $\text{TiO}_2$  can easily be transferred to the VB of  $\text{g-C}_3\text{N}_4$ . Compared with  $\cdot\text{OH}/\text{OH}^-$  (1.99 eV vs. NHE) and  $\cdot\text{OH}/\text{H}_2\text{O}$  (2.68 eV vs. NHE),<sup>11</sup> the reduction potential of the VB of  $\text{g-C}_3\text{N}_4$  is even lower (1.65 eV vs. NHE). Therefore, the holes in the VB of  $\text{g-C}_3\text{N}_4$  can be used to degrade RhB directly. Fig. 11 illustrates the  $\text{La}_x\text{TiCN}$  heterojunction degradation mechanism. The close interface formed by  $\text{TiO}_2$  and  $\text{g-C}_3\text{N}_4$  is a green channel for electron passage, which is beneficial to increase the transfer rate of  $\text{g-C}_3\text{N}_4$  photoelectrons. The proper amount of La is introduced, the interface barrier of La and  $\text{TiO}_2$  becomes higher and the space charge region is narrowed in the system. The generated large electric field promotes the light-induced electron orientation of  $\text{g-C}_3\text{N}_4$  to the interface between La and  $\text{TiO}_2$ , and the electron-hole recombination is effectively prevented in this process. Thus, during the photocatalytic reaction,  $\text{h}^+$  and  $\cdot\text{O}^{2-}$  are the most important active species, which is consistent with the results of the active component trapping experiment. In addition, the hetero interface formed between  $\text{TiO}_2$  and  $\text{g-C}_3\text{N}_4$  can facilitate charge transfer among the particles, and the incorporation of  $\text{La}^{3+}$  can help enhance the electron-hole pair separation efficiency in such a three-way catalytic system and further promote the photocatalytic efficiency.

## 4. Conclusion

$\text{La}_x\text{TiCN}$  heterojunction composites were fabricated successfully using a simple hydrothermal method. The prepared composite catalysts exhibited enhanced photocatalytic activity compared to that of pure  $\text{TiO}_2$  under visible light irradiation for RhB degradation. The tightly connected interface between the  $\text{TiO}_2$  and  $\text{g-C}_3\text{N}_4$  contributed to the stable transmission of photo-generated electrons, and  $\text{La}^{3+}$  could trap electrons, thereby hindering electron-hole recombination. The mutual synergy between the three-way catalytic systems effectively improved the separation efficiency of the electron-hole pairs. The prepared three-dimensional, flower-like  $\text{La}_x\text{TiCN}$  proved capable of exhibiting a strong visible light response and is potential for the removal of environmental pollutants originating from industrial wastewater.

## Conflicts of interest

There are no conflicts to declare.

## Acknowledgements

This work was supported by the Research Project of Education Ministry of Heilongjiang Province of China (YSTSXK201843, 135209223), the Research Innovation Program for College Graduates of Qiqihar University (YJSCX2017-033X) and the Research Project of the Ministry of Human Resources and Social Security of China (2015).

## Notes and references

- 1 T. J. Zhu, J. Li and Q. S. Wu, *ACS Appl. Mater. Interfaces*, 2011, **3**, 3448–3453.
- 2 M. Ahmadi, H. R. Motlagh, N. Jaafarzadeh, A. Mostoufi, R. Saeedi, G. Barzegar and S. Jorfi, *J. Environ. Manage.*, 2017, **186**, 55–63.
- 3 L. Jiang, X. Yuan, Y. Pan, J. Liang, G. Zeng, Z. Wu and H. Wang, *Appl. Catal., B*, 2017, **22**, 388–406.
- 4 K. X. Zhu, W. J. Wang, A. Meng, M. Zhao, J. H. Wang, M. Zhao, D. L. Zhang, Y. P. Jia, C. H. Xu and Z. J. Li, *RSC Adv.*, 2015, **5**, 56239–56243.
- 5 J. Wang, J. Huang, H. Xie and A. Qu, *Introd. Hydrogen Energy*, 2014, **39**, 6354–6363.
- 6 C. S. Selvam and K. J. Wan, *RSC Adv.*, 2016, **6**, 10487–10497.
- 7 J. L. Li, T. Liu, G. Z. Sui and D. S. Zhen, *J. Nanosci. Nanotechnol.*, 2015, **15**, 1408–1415.
- 8 J. Li, E. Liu, Y. Ma, X. Hu, J. Wan, L. Sun and J. Fan, *Appl. Surf. Sci.*, 2016, **364**, 694–702.
- 9 L. J. Zhang, M. X. Li, Q. Y. Li and J. J. Yang, *Appl. Catal., B*, 2017, **212**, 106–114.
- 10 Y. F. Chen, W. X. Huang, D. L. He, Y. Situ and H. Huang, *ACS Appl. Mater. Interfaces*, 2014, **6**, 14405–14414.
- 11 L. Ma, G. H. Wang, C. J. Jiang, H. L. Bao and Q. C. Xu, *Appl. Surf. Sci.*, 2017, **430**, 263–272.
- 12 R. R. Hao, G. H. Wang, C. J. Jiang, H. Tang and Q. C. Xu, *Appl. Surf. Sci.*, 2017, **411**, 400–410.
- 13 K. Wei, K. X. Li, L. S. Yan, S. L. Luo, H. Q. Guo, Y. H. Dai and X. B. Luo, *Appl. Catal., B*, 2018, **222**, 88–98.
- 14 Z. W. Li, G. D. Jiang, Z. H. Zhang, Y. Wu and Y. H. Han, *J. Mol. Catal. A: Chem.*, 2016, **425**, 340–348.
- 15 Y. J. Zou, J. W. Shi, D. D. Ma, Z. Y. Fan, L. Lu and C. m. Niu, *Chem. Eng. J.*, 2017, **322**, 435–444.
- 16 J. L. Li, S. Q. Jia, G. Z. Sui, L. J. Du and B. X. Li, *RSC Adv.*, 2017, **7**, 34857–34865.
- 17 L. Zhou, L. Z. Wang, J. Y. Lei, Y. D. Liu and J. L. Zhang, *Catal. Commun.*, 2016, **89**, 125–128.
- 18 L. Y. Shen, Z. P. Xing, J. L. Zou, Z. Z. Li, X. Y. Wu and Y. C. Zhang, *Sci. Rep.*, 2017, **7**, 41978–41984.
- 19 Z. L. Shi, M. Guo, L. J. Wang and S. H. Yao, *Chin. J. Chem. Phys.*, 2016, **29**, 199–204.
- 20 Q. J. Zhang, Y. Fu, Y. F. Wu and T. Y. Zuo, *Eur. J. Inorg. Chem.*, 2016, **11**, 1706–1711.
- 21 Y. M. Yu, L. J. Piao, J. X. Xia, W. Z. Wang, J. F. Geng, H. Y. Chen, X. Xing and H. Li, *Mater. Chem. Phys.*, 2016, **182**, 77–85.
- 22 X. S. Rong, F. X. Qiu, J. Rong, J. Yan, H. Zhao, X. L. Zhu and D. Y. Yang, *J. Solid State Chem.*, 2015, **230**, 126–134.
- 23 N. R. Khalid, E. Ahmed, Z. L. Hong and M. Ahmad, *Appl. Surf. Sci.*, 2012, **26**, 3254–3259.
- 24 N. Lu, C. H. Wang, B. Sun, Z. M. Gao and Y. Su, *Sep. Purif. Technol.*, 2017, **186**, 226–232.
- 25 D. Xu, L. Feng and A. Lei, *J. Colloid Interface Sci.*, 2009, **329**, 395–403.
- 26 B. Z. Fang, A. Bonakdarpour, K. Reilly, Y. L. Xing, F. Taghipour and D. P. Wilkinson, *ACS Appl. Mater. Interfaces*, 2014, **6**, 15488–15498.





- 27 B. Z. Fang, Y. L. Xing, A. Bonakdarpour, S. C. Zhang and D. P. Wilkinson, *ACS Sustainable Chem. Eng.*, 2015, **3**, 2381–2388.
- 28 Y. Tan, Z. Shu, J. Zhou, T. Li, W. Wang and Z. G. Zhao, *Appl. Catal., B*, 2018, **230**, 260–268.
- 29 Y. N. Li, M. Q. Wang and S. J. Bao, *Ceram. Int.*, 2016, **42**, 18521–18528.
- 30 X. R. Du, G. J. Zou, Z. G. Wang and X. L. Wang, *Nanoscale*, 2015, **7**, 8701–8706.
- 31 K. Dai, L. H. Lu, C. H. Liang, Q. Liu and G. P. Zhu, *Appl. Catal., B*, 2014, **156**, 331–340.
- 32 A. Surendra, B. Sambandamb, T. Pradeepb and L. Philipa, *J. Environ. Chem. Eng.*, 2017, **5**, 757–767.
- 33 S. Zhou, Y. Liu, J. M. Li, Y. J. Wang, G. Y. Jiang, Z. Zhao, D. X. Wang, A. H. Duan, J. Liu and Y. C. Wei, *Appl. Catal., B*, 2014, **158**, 20–29.
- 34 C. Han, Y. D. Wang, Y. P. Lei, B. Wang, N. Wu, Q. Shi and Q. Li, *Nano Res.*, 2015, **8**, 1199–1209.
- 35 Y. Chen, Q. Wu, C. Zhou and Q. T. Jin, *Adv. Powder Technol.*, 2017, **322**, 296–300.
- 36 L. Yu, X. Yang, J. He, Y. He and D. Wang, *J. Alloys Compd.*, 2015, **637**, 308–314.
- 37 J. Su, L. Zhu, P. Geng and G. Chen, *J. Hazard. Mater.*, 2016, **316**, 159–168.
- 38 K. A. Ali, A. Z. Abdullah and A. R. Mohamed, *Appl. Catal., A*, 2017, **537**, 111–120.
- 39 L. Yu, X. Yang, J. He and D. Wang, *J. Alloys Compd.*, 2015, **637**, 308–314.
- 40 M. Wu, M. Zhang, T. Lv, M. Guo, J. Li and C. A. Okonkwo, *Appl. Catal., A*, 2017, **547**, 96–104.
- 41 W. K. Jo and T. S. Natarajan, *Chem. Eng. J.*, 2015, **281**, 549–565.
- 42 M. Q. Sun, S. L. Shen, Z. J. Wu, Z. H. Tang, J. P. Shen and J. H. Yang, *Ceram. Int.*, 2018, **44**, 8125–8132.
- 43 X. S. Zhou, B. Jin, L. D. Li, F. Peng, H. J. Wang, H. Yu and Y. P. Fang, *J. Mater. Chem.*, 2012, **22**, 17900–17905.

